A DISCONTINUOUS GALERKIN METHOD FOR THE EEG FORWARD PROBLEM

CHRISTIAN ENGWER [*†‡§], JOHANNES VORWERK [†¶‖], JAKOB LUDEWIG [‡¶‖], AND CARSTEN H. WOLTERS [¶‖]

Abstract. In order to perform accurate electroencephalography (EEG) source reconstruction, i.e., to localize the sources underlying a measured EEG, the electric potential distribution at the electrodes generated by a dipolar current source in the brain has to be simulated, the so-called EEG forward problem. Therefore, it is necessary to apply numerical methods that are able to take the individual geometry and conductivity distribution of the subject's head into account. The finite element method (FEM) has shown high numerical accuracy with the possibility to model complex geometries and conductive features, e.g., white matter conductivity anisotropy. In this article we introduce and analyze the application of a Discontinuous Galerkin (DG) method, a finite element method that includes features of the finite volume framework, to the EEG forward problem. The DG-FEM approach allows to fulfill the conservation property of electric charge also in the discrete case, making it attractive for a variety of applications. Furthermore, as we show, it can alleviate modeling inaccuracies that might occur in head geometries when using classical FE methods, e.g., so-called "skull leakage effects" for skull compartments with a thickness in the range of the mesh resolution. Therefore, we derive a DG formulation of the FEM subtraction approach for the EEG forward problem and present first numerical results which highlight the advantageous features and the potential of the proposed approach.

Key words. discontinuous Galerkin, finite element method, conservation properties, EEG, dipole, subtraction method, four layer sphere model

AMS subject classifications. 35J25, 35J75, 35Q90, 65N12, 65N30, 68U20, 92C50

1. Introduction. EEG source reconstruction is nowadays widely used in both research and clinical routine to measure the electrical activity in the human brain, as it is a non-invasive, easy to perform, and relatively cheap technique [29, 16]. To reconstruct the active brain areas from the electric potentials measured at the head surface, it is necessary to simulate the electric potential generated by a dipolar current source in the grey matter compartment of the brain, the so-called EEG forward problem. The achievable accuracy in solving the forward problem strongly depends on a realistic modeling of shape and conductive features of the volume conductor, i.e., the human head. Therefore, it is necessary to apply numerical methods to solve the underlying partial differential equations in realistic geometries, since analytical solutions only exist for few special cases, e.g., nested shells [20]. Different numerical methods have been proposed to solve this problem, e.g., boundary element methods (BEM) [33, 1, 27, 45], finite volume methods (FVM) [19], finite difference methods (FDM) [54, 49, 32] or finite element methods (FEM) [12, 31, 41, 23, 36, 35]. Finite element methods were shown to achieve high numerical accuracies [23, 51], while the

[*]Corresponding author: christian.engwer@uni-muenster.de

[†]The first two authors contributed equally to this work.

[‡]Institute for Computational and Applied Mathematics, University of Münster, Einsteinstraße 62, 48149 Münster, Germany

[§]Cluster of Excellence EXC 1003, Cells in Motion, CiM, Mnster, Germany

[¶]Institute for Biomagnetism and Biosignalanalysis, University of Münster, Malmedyweg 15, 48149 Münster, Germany

[‖]This work was partially supported by the Priority Program 1665 of the Deutsche Forschungsgemeinschaft (DFG) (WO1425/5-1), the Cluster of Excellence 1003 of the Deutsche Forschungsgemeinschaft (DFG EXC 1003 Cells in Motion) and by EU project ChildBrain (Marie Curie Innovative Training Networks, grant agreement no. 641652).

computational burden could be clearly reduced by the introduction of transfer matrices and fast solver methods [53, 25, 57]. They offer the important possibility to model complex geometries and also anisotropic conductivities, with only weak influence on the computational effort [50].

One of the main tasks in applying FEM to solve the EEG forward problem is to deal with the strong singularity introduced by the source model of a current dipole. Therefore, different approaches to solve the EEG forward problem using FEM have been proposed, e.g., the Saint-Venant [47, 43, 17, 51], the partial integration [60, 53, 48, 51], the Whitney or Raviart-Thomas [46, 35] or the subtraction approach [12, 31, 41, 59, 23, 51]. All of these approaches rely on a Continuous Galerkin FEM (CG-FEM) formulation, also called Lagrange- or conforming FEM, i.e., the resulting solution for the electric potential is continuous.

The use of tetrahedral [31, 23, 50] as well as that of hexahedral [41, 38, 6, 5] meshes has been proposed for solving the EEG forward problem with the FEM. Tetrahedral meshes can be generated by Constrained Delaunay tetrahedralizations (CDT) from given tissue surface representations [23, 50]. This has the advantage that smooth tissue surfaces are well represented in the model. On the other side, the generation of such models is difficult in practice and might cause unrealistic model features, e.g., holes in tissue compartments such as the foramen magnum and the optic canals in the skull are often artificially closed to allow CDT meshing. Furthermore, CDT modeling necessitates nested surfaces, while in reality surfaces might touch like for example the inner skull and outer brain surface. Hexahedral models do not suffer from such limitations, can be easily generated from voxel-based magnetic resonance imaging (MRI) data and are more and more frequently used in source analysis applications [38, 6, 5]. This paper therefore focuses on hexahedral FEM approaches. However, the application of the CG-FEM with hexahedral meshes has the disadvantage that the representation of thin tissue structures in combination with insufficient mesh resolutions might result in geometry approximation errors. It has, e.g., been shown in [44] that the combination of thin skull structures and insufficient hexahedral mesh resolutions might result in so-called skull-leakages in areas where scalp and CSF elements are erroneously connected via single skull vertices or edges as illustrated in Figure 2.1. This can lead to significantly inaccurate results when using vertex based methods like, e.g., CG-FEM, and might be one of the main reasons why in a recent head modeling comparison study for EEG source analysis in presurgical epilepsy diagnosis a 2 mm hexahedral FEM approach did not perform better than simpler head models [13].

In this paper, we derive the mathematical equations underlying the forward problem of EEG and introduce its solution using the subtraction approach. After a short explanation of strengths and weaknesses of this solution approach, we propose and evaluate a new formulation of the subtraction approach on the basis of Discontinuous Galerkin FEM (DG-FEM). We then show that, while CG- and DG-FEM achieve similar numerical accuracies in multi-layer sphere validation studies with high mesh resolutions, DG-FEM mitigates the problem of skull leakages in case of lower resolutions.

2. Theory.

2.1. The forward problem. The partial differential equation underlying the forward problem can be derived by introducing the quasi-static approximation of Maxwell's equations [29, 16]. When relating the electric field to a scalar potential, $E = -\nabla u$, and splitting up the current density J into a term f, which describes the current source and a return current, or flux, $-\sigma\nabla u$ with $\sigma(x)$ being the conductivity

distribution in the head domain, we get a *Poisson equation*

$$-\nabla \cdot (\sigma \nabla u) = f \qquad \text{in } \Omega, \tag{2.1a}$$

$$\sigma \partial_{\mathbf{n}} u = 0 \qquad \text{on } \partial\Omega = \Gamma, \tag{2.1b}$$

where Ω denotes the head domain, which is assumed to be open and connected, and Γ its boundary. We have homogeneous Neumann boundary conditions here, since we assume a conductivity $\sigma(x) = 0$ for all $x \notin \bar{\Omega}$.

2.2. The Subtraction approach. We briefly derive the classical subtraction FE approach as presented in [59, 23]. We assume the commonly used point-like dipole source at position y with moment p, $f_y(x) = \nabla \cdot (p\delta_y(x))$. This complicates the further mathematical treatment, as the right-hand-side is not even square-integrable in this case. However, when assuming that there exists a non-empty open neighborhood Ω^∞ of the source position y with constant isotropic conductivity σ^∞, we can split up the potential u and the conductivity σ into two parts:

$$u = u^\infty + u^{\text{corr}}, \tag{2.2a}$$

$$\sigma = \sigma^\infty + \sigma^{\text{corr}}. \tag{2.2b}$$

u^∞ is the potential in an unbounded, homogeneous conductor and can be calculated analytically: $u^\infty(x) = \frac{1}{4\pi\sigma^\infty} \frac{\langle p, x-y \rangle}{|x-y|^3}$. The more general case of anisotropic conductivities can be treated, too [59, 23], but is not especially derived here.

Inserting the decomposition of u into (2.1) and subtracting the homogeneous solution, again results in a Poisson equation for the searched correction potential u^{corr}:

$$-\nabla \cdot (\sigma \nabla u^{\text{corr}}) = \nabla \cdot (\sigma^{\text{corr}} \nabla u^\infty) \quad \text{in } \Omega, \tag{2.3a}$$

$$\sigma \partial_{\mathbf{n}} u^{\text{corr}} = -\sigma \partial_{\mathbf{n}} u^\infty \quad \text{on } \Gamma. \tag{2.3b}$$

To solve this problem numerically, [23] propose a conforming first-order finite element method: Find $u^{\text{corr}} \in V_h \subset H^1$ such that it fulfills the weak formulation

$$\int_\Omega \sigma \nabla u^{\text{corr}} \cdot \nabla v dx = -\int_\Omega \sigma^{\text{corr}} \nabla u^\infty \cdot \nabla v dx - \int_{\partial\Omega} \sigma^\infty \partial_{\mathbf{n}} u^\infty \cdot v ds. \tag{2.4}$$

The weak form can be heuristically derived by multiplication with a test function $v \in V_h$ and subsequent partial integration. Reorganization of some terms and applying the identity (2.2b) yields the proposed form in equation (2.4). The subtraction approach is theoretically well understood, existence and uniqueness of a solution as well as convergence of the numerical solution are examined in [59, 23].

2.3. Skull leakage effects. As discussed in the introduction, hexahedral meshes are frequently used in practical applications of FEM-based EEG/MEG source analysis, due to the clearly simplified creation process in comparison to CDT meshes. A pitfall that has to be taken into account in this scenario are leakage effects, especially in the thin skull compartment. If the resolution is coarse compared to the thickness of the skull, segmentation artifacts as illustrated in Figure 2.1 (yellow and red line) occur. Although physically separated, elements belonging to the highly conductive compartments interior to the skull, i.e., most often the CSF, and to the skin compartment are now connected via a shared vertex or edge. When using, e.g., the CG-FEM

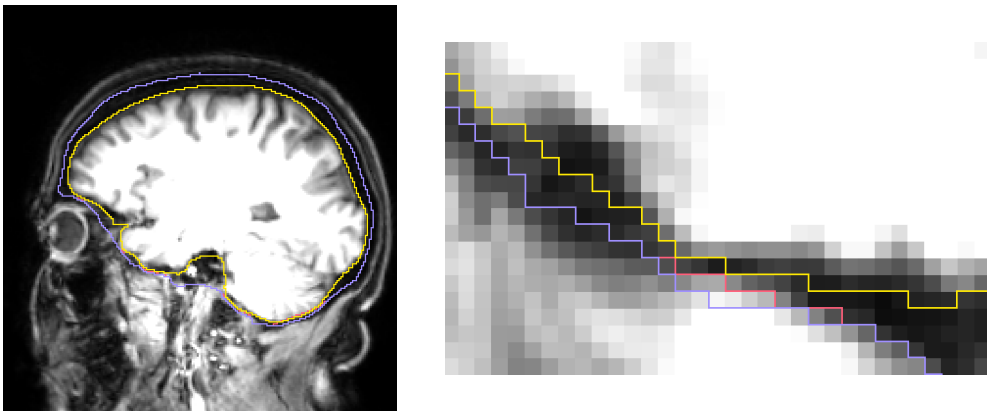

FIG. 2.1. *Sketch of segmentation that might lead to leakage effects (left). Yellow line shows inner skull surface, red line original outer skull surface, blue line corrected outer skull surface. Where red and blue line overlap, only blue line is visible. In the magnified detail scalp and CSF show two erroneous connections via single vertices or edges (right subfigure, where red and yellow lines touch each other). This can lead to significantly inaccurate results when using vertex based methods like, e.g., CG-FEM.*

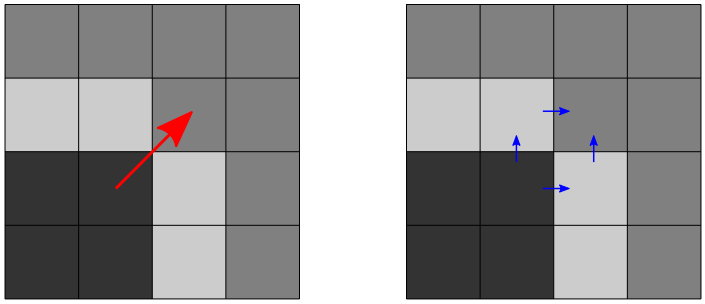

FIG. 2.2. *CG-FEM simulations lead to an overestimated electric current at degenerated vertices of the skull. This is due to the vertex based discretization, which only considers the potential, but not the electric current. DG-FEM methods are based on a current reconstruction through cell faces. Thereby, these methods do not overestimate the electric current, even in the presence of imaging artifacts.*

with Lagrange Ansatz functions, these artifacts lead to skull leakage, as sketched in Figure 2.2. As a result of the vertex based Ansatz-functions, this leads to inadequately high matrix entries for these vertices and finally to current leakage "through" these vertices.

This problem might be circumvented by artificially increasing the thickness of the modeled skull in these areas (blue line in Figure 2.1). However, this might, again, lead to inaccuracies in the EEG forward computation due to the now too thick skull compartment.

In the following, we derive a Discontinuous Galerkin (DG) formulation for the Subtraction FE approach. This has the advantageous feature of being locally charge preserving and controlling for the current flow through element faces, thereby preventing possible leakage effects, see illustration in Figure 2.2.

2.4. A Discontinuous Galerkin formulation. Preserving fundamental physical properties is very important in order to get a good interpretation of the simulation results. As discussed in the previous section a correct approximation of the electric current is crucial to gain reliable simulation results. Continuity of the current directly implies conservation of charge.

The Discontinuous Galerkin method allows to construct formulations which preserve such conservation properties also in the discretized space. We first discuss which quantities to preserve when using the subtraction approach for the continuous problem and then introduce a Discontinuous Galerkin formulation.

2.4.1. Conservation properties. A fundamental physical property is the conservation of charge. The conservation of charge is equivalent to the continuity of the electric current:

$$\int_{\partial K} \sigma \nabla u \cdot \vec{n}\, ds = \int_K f_y dx, \tag{2.5}$$

for any control volume $K \subseteq \Omega$. Following the subtraction approach we split the current $\sigma\nabla u = (\sigma^\infty + \sigma^{\text{corr}})\nabla(u^\infty + u^{\text{corr}})$. Rearrangement then yields

$$\int_{\partial K} \sigma \nabla u^{\text{corr}} \cdot \vec{n}\, ds = -\int_{\partial K} \sigma^{\text{corr}} \nabla u^\infty \cdot \vec{n}\, dx \underbrace{- \int_{\partial K} \sigma^\infty \nabla u^\infty \cdot \vec{n}\, ds + \int_K f_y dx}_{\equiv 0}\,.$$

Applying Gauss' theorem to the right hand side, we obtain a conservation property for the correction potential

$$\int_{\partial K} \underbrace{\sigma \nabla u^{\text{corr}}}_{\vec{j}^{\text{corr}}} \cdot \vec{n}\, ds = \int_K \underbrace{-\nabla \cdot \sigma^{\text{corr}} \nabla u^\infty}_{f^{\text{corr}}} dx\,, \tag{2.6}$$

which basically states that u^{corr} is a conserved property with flux $\vec{j}^{\text{corr}} = \sigma\nabla u^{\text{corr}}$ and a source term $f^{\text{corr}} = \nabla \cdot \sigma^{\text{corr}} \nabla u^\infty$.

For FEM this property carries over to the discrete solution, if the test space contains the characteristic function, which is one on K and zero everywhere else. In general, a conforming discretization does not guarantee this property, as it is not possible to construct the appropriate test function for a single cell , for $K = \Omega$ it is only possible for pure Neumann boundary conditions.

Conservation of charge also holds for u^∞ in the case of a homogeneous volume conductor (with conductivity σ^∞ in our case). Thus both the electrical flux $\sigma\nabla u$ and $\sigma^\infty \nabla u^\infty$ are continuous. Rewriting $\vec{j}$ in terms of σ^{corr}, σ^∞, u^{corr} and u^∞ we can show that also $\sigma\nabla u^{\text{corr}} + \sigma^{\text{corr}}\nabla u^\infty$ is continuous.

DEFINITION 2.1. *We consider an arbitrary interface γ, which separates the control volume K into two patches K_l and K_r (see Figure 2.3). The jump of a function u along γ is given as*

$$[u](x) = \lim_{x' \to x \text{ in } K_l} u(x') - \lim_{x' \to x \text{ in } K_r} u(x') \tag{2.7}$$

LEMMA 2.2. *Given a potential u with a continuous flux $\sigma\nabla u$, also $\sigma\nabla u^{corr} + \sigma^{corr}\nabla u^\infty$ is continuous for the subtraction approach.*

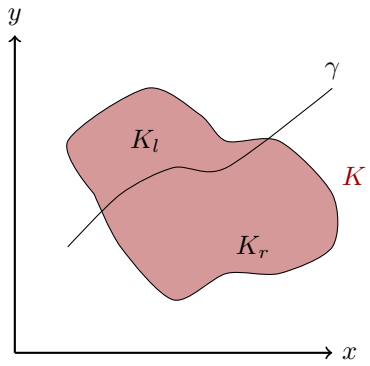

FIG. 2.3. *Interface γ splits K into two parts.*

Proof. We consider an arbitrary interface γ. At each point x along γ the fluxes $\sigma\nabla u$ and $\sigma^\infty\nabla u^\infty$ are continuous. Thus the jump vanishes for them and we obtain

$$[\sigma\nabla u] = 0 = [\sigma^\infty\nabla u^\infty]. \tag{2.8}$$

Rewriting $[\sigma\nabla u]$ in terms of $\sigma^{\text{corr}}, \sigma^\infty, u^{\text{corr}}$, and u^∞ we obtain

$$\begin{aligned} &\Leftrightarrow [\sigma^\infty\nabla u^{\text{corr}}] + [\sigma^{\text{corr}}\nabla u^{\text{corr}}] + [\sigma^{\text{corr}}\nabla u^\infty] = 0 \\ &\Leftrightarrow \qquad [\sigma\nabla u^{\text{corr}}] = -[\sigma^{\text{corr}}\nabla u^\infty] \\ &\Leftrightarrow \qquad [\sigma\nabla u^{\text{corr}} + \sigma^{\text{corr}}\nabla u^\infty] = 0. \end{aligned} \tag{2.9}$$

As this property holds for any control volume and for any interface γ the combined flux $\sigma\nabla u^{\text{corr}} + \sigma^{\text{corr}}\nabla u^\infty$ is also continuous. ∎

Note that this also implies the identity

$$[\sigma\nabla u^{\text{corr}}] = -[\sigma^{\text{corr}}\nabla u^\infty]\,, \tag{2.10}$$

which is later needed to derive the weak form (2.21) out of equations (2.19) and (2.20).

2.4.2. A weak formulation. An alternative to the conforming discretization sketched in Section 2.2 is to use more general trial and test spaces. In the following section we derive a discontinuous Galerkin discretization for the subtraction approach to solve the EEG forward problem. We assume knowledge about the basic FE theory, see e.g. [15, 28]. For DG methods we furthermore refer to [3] or the book of Pietro and Ern [21]. After the definition of broken polynomial spaces, we derive a locally conservative weak formulation of the subtraction approach and introduce stabilisation terms to guarantee existence and uniqueness of the solution.

DEFINITION 2.3 (Triangulation $\mathcal{T}_h(\Omega)$). *Let $\mathcal{T}_h(\Omega)$ be a finite collection of disjoint and open subsets forming a partition of Ω. The subscript h corresponds to the mesh-width $h := \max\{diam(E) \mid E \in \mathcal{T}_h\}$.* Furthermore the triangulation induces the *internal skeleton*

$$\Gamma_{\text{int}} = \{\gamma_{e,f} = \partial E_e \cap \partial E_f \mid E_e, E_f \in \mathcal{T}_h\,,\, E_e \neq E_f,\, |\gamma_{e,f}| > 0\} \tag{2.11}$$

and the *skeleton* $\Gamma = \Gamma_{\text{int}} \cup \partial\Omega$.

DEFINITION 2.4 (Broken polynomial spaces). *Broken polynomial spaces are defined as piece-wise polynomial spaces on the partition $\mathcal{T}_h(\Omega)$ as*

$$V_h^k = \left\{\, v \in L^2(\Omega) \,:\, v|_E \in P^k(E) \,\right\} \tag{2.12}$$

where P^k denotes the space of polynomial functions of degree k. They describe functions which exhibit element-wise polynomial behaviour but may be discontinuous across element interfaces.

Using a Galerkin approach, we seek for a solution $u_h^{\text{corr}} \in V_h^k$, which fulfils (2.3) in a weak sense. We start the derivation by testing with a test function $v_h \in V_h^k$:

$$-\int_\Omega \nabla \cdot \sigma \nabla u_h^{\text{corr}} v_h \, dx = \int_\Omega \nabla \cdot \sigma^{\text{corr}} \nabla u^\infty v_h \, dx \tag{2.13}$$

On each $E \in \mathcal{T}_h(\Omega)$ we apply integration by parts. For the left hand side we obtain

$$\begin{aligned}
\text{lhs} &= -\int_\Omega \nabla \cdot \sigma \nabla u_h^{\text{corr}} v_h \, dx \\
&= -\sum_{E_e \in \mathcal{T}_h} \int_{E_e} \nabla \cdot \sigma \nabla u_h^{\text{corr}} v_h \, dx \\
&= \int_\Omega \sigma \nabla u_h^{\text{corr}} \cdot \nabla v_h \, dx - \sum_{E_e \in \mathcal{T}_h} \int_{\partial E_e} \sigma \nabla u_h^{\text{corr}} \cdot \vec{n} \, v_h \, ds \\
&= \int_\Omega \sigma \nabla u_h^{\text{corr}} \cdot \nabla v_h \, dx - \int_{\partial\Omega} \underbrace{\sigma \nabla u_h^{\text{corr}} \cdot \vec{n}}_{= -\sigma \nabla u^\infty \cdot \vec{n} \ \text{(2.3b)}} v_h \, ds \\
&\quad - \sum_{\gamma_{e,f} \in \Gamma_{\text{int}}} \left(\int_{\gamma_{e,f} \cap \partial E_e} \sigma \nabla u_h^{\text{corr}} \cdot \vec{n}_{e,f} v_h \, ds + \int_{\gamma_{e,f} \cap \partial E_f} \sigma \nabla u_h^{\text{corr}} \cdot \vec{n}_{f,e} v_h \, ds \right),
\end{aligned} \tag{2.14}$$

where $\vec{n}_{e,f}$ denotes the outwards pointing normal unit vector on the boundary of E_e, pointing from E_e to E_f.

The sum over all element boundaries is split up into the domain boundary and all internal edges, each being visited twice, once from left and once from right. The electrical current $\sigma \nabla u_h^{\text{corr}} \cdot \vec{n}$ through the boundary is given by the inhomogeneous Neumann boundary conditions (2.3b).

Following the notation of [3] we introduce the *jump operator*

$$[\![x]\!]_{e,f} \;=\; x|_{\partial E_e} \vec{n}_{e,f} \;+\; x|_{\partial E_f} \vec{n}_{f,e} \tag{2.15}$$

and the *average operator*

$$\langle x \rangle_{e,f} := \omega_{e,f} x|_{\partial E_e} + \omega_{f,e} x|_{\partial E_f} \tag{2.16}$$

of a piecewise continuous function x on the interface $\gamma_{e,f}$ between two adjacent elements E_e and E_f. The weights $\omega_{e,f}$ and $\omega_{f,e}$ can be chosen to be the arithmetic mean, but for the case of heterogeneous conductivities [24] has shown that a conductivity-dependent choice is optimal:

$$\omega_{e,f} := \frac{\sigma_f}{\sigma_f + \sigma_e} \quad \text{and} \quad \omega_{f,e} := \frac{\sigma_e}{\sigma_e + \sigma_f}\,. \tag{2.17}$$

Jump and average fulfill the following multiplicative property

$$[\![xy]\!]_{e,f} = [\![x]\!]_{e,f} \langle y \rangle_{e,f} + \langle x \rangle_{e,f} [\![y]\!]_{e,f}\,. \tag{2.18}$$

We now rewrite (2.14) and obtain

$$\text{lhs} = \int_\Omega \sigma \nabla u_h^{\text{corr}} \cdot \nabla v_h \, dx + \int_{\partial\Omega} \sigma \nabla u^\infty \cdot \vec{n} \, v_h \, ds - \int_{\Gamma_{\text{int}}} [\![\sigma \nabla u_h^{\text{corr}} v_h]\!] \, ds$$

and with the multiplicative property (2.18) follows

$$\begin{aligned} \text{lhs} = \int_\Omega \sigma \nabla u_h^{\text{corr}} \cdot \nabla v_h \, dx + \int_{\partial\Omega} \underbrace{\sigma \nabla u^\infty \cdot \vec{n} \, v_h}_{\text{term } \dagger} \, ds \\ - \int_{\Gamma_{\text{int}}} \underbrace{[\![\sigma \nabla u_h^{\text{corr}}]\!]}_{\text{term } \ddagger} \langle v_h \rangle + \langle \sigma \nabla u_h^{\text{corr}} \rangle [\![v_h]\!] \, ds \,. \end{aligned} \tag{2.19}$$

Applying the same relations for the right hand side we obtain

$$\begin{aligned} \text{rhs} = - \int_\Omega \sigma^{\text{corr}} \nabla u^\infty \cdot \nabla v_h \, dx + \int_{\partial\Omega} \underbrace{\sigma^{\text{corr}} \nabla u^\infty \cdot \vec{n} \, v_h}_{\text{term } \dagger} \, ds \\ + \int_{\Gamma_{\text{int}}} \underbrace{[\![\sigma^{\text{corr}} \nabla u^\infty]\!]}_{\text{term } \ddagger} \langle v_h \rangle + \langle \sigma^{\text{corr}} \nabla u^\infty \rangle [\![v_h]\!] \, ds \,. \end{aligned} \tag{2.20}$$

Summing up the boundary integrals $(2.19)^\dagger$ and $(2.20)^\dagger$ yields a remaining term $-\sigma^\infty \nabla u^\infty \cdot \vec{n} \, v_h$ on the rhs. As discussed in Section 2.4.1 the conservation properties also imply that $\sigma \nabla u^{\text{corr}} + \sigma^{\text{corr}} \nabla u^\infty$ is continuous, see (2.9). For the discrete solution we require the same conservation property, thus the jump term $(2.19)^\ddagger$ equals to $-[\![\sigma^{\text{corr}} \nabla u^\infty]\!]$ and cancels out with term $(2.20)^\ddagger$.

We obtain the following weak formulation:
Find $u_h^{\text{corr}} \in V_h^k(\Omega)$ such that

$$\tilde{a}(u_h^{\text{corr}}, v_h) = l(v_h) \qquad \text{for all } v_h \in V_h^k(\Omega) \tag{2.21}$$

with

$$\begin{aligned} \tilde{a}(u_h^{\text{corr}}, v_h) = & \int_\Omega \sigma \nabla u_h^{\text{corr}} \cdot \nabla v_h \, dx - \int_{\Gamma_{\text{int}}} \langle \sigma \nabla u_h^{\text{corr}} \rangle [\![v_h]\!] \, ds \,, \\ l(v_h) = & - \int_\Omega \sigma^{\text{corr}} \nabla u^\infty \cdot \nabla v_h \, dx \\ & - \int_{\partial\Omega} \sigma^\infty \partial_{\mathbf{n}} u^\infty v_h \, ds + \int_{\Gamma_{\text{int}}} \langle \sigma^{\text{corr}} \nabla u^\infty \rangle [\![v_h]\!] \, ds \,. \end{aligned}$$

While the formulation derived in this fashion is by construction consistent with the strong formulation (2.3), the method does not show adjoint consistency and is not stable since it lacks coercivity. As discussed in [3], consistency of the adjoint problem is important to ensure conservation properties, in our case Equation (2.6), coercivity is necessary to ensure existence and uniqueness of the solution.

To gain adjoint consistency we symmetrize the operator and add the additional term

$$\tilde{a}^{\text{sym}}(u_h^{\text{corr}}, v_h) := - \int_{\Gamma_{\text{int}}} \langle \sigma \nabla v_h \rangle [\![u_h^{\text{corr}}]\!] \, ds \,. \tag{2.22}$$

To obtain coercivity the left hand side is supplemented with the penalty term

$$J(u_h^{\mathrm{corr}}, v_h) = \eta \int_{\Gamma_{\mathrm{int}}} \frac{\hat{\sigma}_\gamma}{h_\gamma} [\![u_h^{\mathrm{corr}}]\!][\![v_h]\!] \, ds \,, \tag{2.23}$$

where h_γ and $\hat{\sigma}_\gamma$ denote local definitions of the mesh width and the electric conductivity on an edge γ, respectively. In our particular case we choose h_γ according to [26] and $\hat{\sigma}_\gamma$ as the harmonic average of the conductivities of the adjacent elements [24]:

$$h_{\gamma_{e,f}} = \frac{\min(|E_e|, |E_f|)}{|\gamma_{e,f}|} \quad \text{and} \quad \hat{\sigma}_{\gamma_{e,f}} := \frac{2\sigma_e \sigma_f}{\sigma_e + \sigma_f} \,.$$

The penalty parameter η has to be chosen large enough to ensure coercivity.

This yields the *Symmetric Interior Penalty Galerkin* (SIPG) formulation [55, 37] or for weighted averages the *Symmetric Weighted Interior Penalty Galerkin* (SWIPG or SWIP) method [24]. The formulation is coercive, consistent, and adjoint consistent. The first two are shown in the next section. The latter is important in the context of inverse problems, like source analysis [39].

The SIPG formulation for the subtraction approach now reads:
Find $u_h^{\mathrm{corr}} \in V_h$ such that

$$a(u_h^{\mathrm{corr}}, v_h) + J(u_h^{\mathrm{corr}}, v_h) = l(v_h) \quad \text{for all } v_h \in V_h. \tag{2.24a}$$

with

$$\begin{aligned} a(u_h^{\mathrm{corr}}, v_h) &= \tilde{a}(u_h^{\mathrm{corr}}, v_h) + \tilde{a}^{\mathrm{sym}}(u_h^{\mathrm{corr}}, v_h) \\ &= \int_\Omega \sigma \nabla u_h^{\mathrm{corr}} \cdot \nabla v_h \, dx - \int_{\Gamma_{\mathrm{int}}} \langle \sigma \nabla u_h^{\mathrm{corr}} \rangle [\![v_h]\!] + \langle \sigma \nabla v_h \rangle [\![u_h^{\mathrm{corr}}]\!] \, ds \,, \end{aligned} \tag{2.24b}$$

$$J(u_h^{\mathrm{corr}}, v_h) = \eta \int_{\Gamma_{\mathrm{int}}} \frac{\hat{\sigma}_\gamma}{h_\gamma} [\![u_h^{\mathrm{corr}}]\!][\![v_h]\!] \, ds \,, \tag{2.24c}$$

$$\begin{aligned} l(v) = &- \int_\Omega \sigma^{\mathrm{corr}} \nabla u^\infty \cdot \nabla v_h \, dx \\ &+ \int_{\Gamma_{\mathrm{int}}} \langle \sigma^{\mathrm{corr}} \nabla u^\infty \rangle [\![v_h]\!] \, ds - \int_{\partial\Omega} \sigma^\infty \partial_{\mathbf{n}} u^\infty v_h \, ds \,. \end{aligned} \tag{2.24d}$$

Given the correction potential u_h^{corr}, the full potential u_h can be reconstructed as $u_h = u_h^{\mathrm{corr}} + u^\infty$.

2.5. Discrete properties. LEMMA 2.5 (Existence and uniqueness). *For a sufficiently large constant $\eta > 0$ the SIPG discretization* (2.24) *has a unique solution.*

Proof. As $a(u_h^{\mathrm{corr}}, v_h)$ and $J(u_h^{\mathrm{corr}}, v_h)$ are the same operators as in [24] the operator $a(u_h^{\mathrm{corr}}, v_h) + J(u_h^{\mathrm{corr}}, v_h)$ is coercive for sufficiently large $\eta > 0$, i.e.,

$$a(v_h, v_h) + J(v_h, v_h) \geq \kappa \|v_h\|_V^2 \qquad \text{for all } v_h \in V_h^k.$$

From coercivity follows existence and as (2.24) is a linear problem existence is equivalent to uniqueness. ∎

LEMMA 2.6 (Consistency). *The SIPG discretization* (2.24) *for the subtraction approach is consistent with the strong problem* (2.3).

Proof. For a solution u of (2.3) u^{corr} is continuous, i.e., $u^{\mathrm{corr}} \in C^0$, and the jump $[\![u^{\mathrm{corr}}]\!]$ vanishes, so that $\tilde{a}^{\mathrm{sym}}(u^{\mathrm{corr}}, v_h) = 0$ in (2.22) and $J(u^{\mathrm{corr}}, v_h) = 0$ in (2.23). Using (2.3b), partial integration and (2.3a), Equation (2.24) reduces to

$$
\begin{aligned}
& a(u^{\mathrm{corr}}, v_h) - l(v_h) \\
&\quad = \int_\Omega \sigma \nabla u^{\mathrm{corr}} \cdot \nabla v_h \, dx - \int_{\Gamma_{\mathrm{int}}} \langle \sigma \nabla u^{\mathrm{corr}} \rangle [\![v_h]\!] \, ds \\
&\qquad + \int_\Omega \sigma^{\mathrm{corr}} \nabla u^\infty \cdot \nabla v_h \, dx - \int_{\Gamma_{\mathrm{int}}} \langle \sigma^{\mathrm{corr}} \nabla u^\infty \rangle [\![v_h]\!] \, ds \\
&\qquad + \int_{\partial\Omega} \sigma^\infty \partial_{\mathbf{n}} u^\infty v_h \, ds \\
&\quad \underset{(2.3b)}{=} \int_\Omega \sigma \nabla u^{\mathrm{corr}} \cdot \nabla v_h \, dx - \int_\Gamma \langle \sigma \nabla u^{\mathrm{corr}} \rangle [\![v_h]\!] \, ds \\
&\qquad + \int_\Omega \sigma^{\mathrm{corr}} \nabla u^\infty \cdot \nabla v_h \, dx - \int_\Gamma \langle \sigma^{\mathrm{corr}} \nabla u^\infty \rangle [\![v_h]\!] \, ds
\end{aligned}
$$

We use (2.9), add $0 = -\int_\Gamma [\![\sigma \nabla u^{\mathrm{corr}}]\!] \langle v_h \rangle \, ds - \int_\Gamma [\![\sigma^{\mathrm{corr}} \nabla u^\infty]\!] \langle v_h \rangle \, ds$ and get

$$
\begin{aligned}
&\quad = \int_\Omega \sigma \nabla u^{\mathrm{corr}} \cdot \nabla v_h \, dx - \int_\Gamma \langle \sigma \nabla u^{\mathrm{corr}} \rangle [\![v]\!] + [\![\sigma \nabla u^{\mathrm{corr}}]\!] \langle v_h \rangle \, ds \\
&\qquad + \int_\Omega \sigma^{\mathrm{corr}} \nabla u^\infty \cdot \nabla v_h \, dx - \int_\Gamma \langle \sigma^{\mathrm{corr}} \nabla u^\infty \rangle [\![v]\!] + [\![\sigma^{\mathrm{corr}} \nabla u^\infty]\!] \langle v_h \rangle \, ds \\
&\quad \underset{(2.18)}{=} \int_\Omega \sigma \nabla u^{\mathrm{corr}} \cdot \nabla v_h \, dx - \int_\Gamma [\![\sigma \nabla u^{\mathrm{corr}} v_h]\!] \, ds \\
&\qquad + \int_\Omega \sigma^{\mathrm{corr}} \nabla u^\infty \cdot \nabla v_h \, dx - \int_\Gamma [\![\sigma^{\mathrm{corr}} \nabla u^\infty v_h]\!] \, ds \\
&\quad = - \int_\Omega \nabla \cdot (\sigma \nabla u^{\mathrm{corr}}) v_h \, dx - \int_\Omega \nabla \cdot (\sigma^{\mathrm{corr}} \nabla u^\infty) v_h \, dx \\
&\quad \underset{(2.3a)}{=} 0
\end{aligned}
$$

Thus u is also a solution of the weak formulation (2.24). ∎

LEMMA 2.7 (Discrete conservation property). *The SIPG discretization* (2.24) *fulfills the discrete conservation property* $\int_{\partial K} \vec{j}_h^{corr} \cdot \vec{n} \, ds = \int_K f^{corr} \, dx$ *which converges to* (2.6).

Proof. Testing with $v_h = 1$ on a control volume $K \in \mathcal{T}_h(\Omega)$ and 0 everywhere else, we observe that inside K, $\nabla v = 0$ and $[\![v]\!] = \vec{n}$ on ∂K. The boundary ∂K is partitioned into boundary facets $\partial K \cap \partial\Omega$ and internal facets $\partial K \setminus \partial\Omega$. With this

(2.24) simplifies to

$$
\begin{aligned}
& a(u_h^{\mathrm{corr}}, v_h) + J(u_h^{\mathrm{corr}}, v_h) = l(v_h) \\
\Leftrightarrow \qquad & -\int_{\partial K \setminus \partial\Omega} \langle \sigma \nabla u_h^{\mathrm{corr}} \rangle \cdot \vec{n}\, ds + \int_{\partial K} \eta \frac{\hat{\sigma}_\gamma}{\hat{h}_\gamma} [\![u_h^{\mathrm{corr}}]\!]\, ds = \\
& \qquad + \int_{\partial K \setminus \partial\Omega} \langle \sigma^{\mathrm{corr}} \nabla u^\infty \rangle \cdot \vec{n}\, ds - \int_{\partial K \cap \partial\Omega} \sigma^\infty \nabla u^\infty \cdot \vec{n}\, ds
\end{aligned}
$$

We exploit $\int_{\partial_K \setminus \partial\Omega} \cdot\, ds = \int_{\partial\Omega} \cdot\, ds - \int_{\partial K \cup \partial\Omega} \cdot\, ds$ and (as $\sigma^\infty \nabla u^\infty$ is continuous) $\langle \sigma^{\mathrm{corr}} \nabla u^\infty \rangle + \sigma^\infty \nabla u^\infty = \langle \sigma \nabla u^\infty \rangle$, rearrange terms and get

$$
\begin{aligned}
\Leftrightarrow \qquad & -\int_{\partial K \setminus \partial\Omega} \langle \sigma \nabla u_h^{\mathrm{corr}} \rangle \cdot \vec{n}\, ds + \int_{\partial K \cap \partial\Omega} \langle \sigma \nabla u^\infty \rangle \cdot \vec{n}\, ds \\
& \qquad + \int_{\partial K} \eta \frac{\hat{\sigma}_\gamma}{\hat{h}_\gamma} [\![u_h^{\mathrm{corr}}]\!]\, ds = \int_{\partial K} \langle \sigma^{\mathrm{corr}} \nabla u^\infty \rangle \cdot \vec{n}\, ds.
\end{aligned}
$$

As σ^{corr} is continuous on K and using the boundary condition (2.3b), we obtain the discrete conservation property

$$
\Leftrightarrow \qquad \int_{\partial K} \underbrace{\langle \sigma \nabla u_h^{\mathrm{corr}} \rangle - \eta \frac{\hat{\sigma}_\gamma}{\hat{h}_\gamma} [u_h^{\mathrm{corr}}]}_{\vec{j}_h^{\mathrm{corr}}} \cdot \vec{n}\, ds = \int_K \underbrace{-\nabla \sigma^{\mathrm{corr}} \nabla u^\infty}_{f^{\mathrm{corr}}}\, ds
$$

The discrete problem (2.24) fulfills the discrete conservation property with a discrete flux $\vec{j}_h^{\mathrm{corr}} = \langle \sigma \nabla u_h^{\mathrm{corr}} \rangle - \eta \frac{\hat{\sigma}_\gamma}{\hat{h}_\gamma} [u_h^{\mathrm{corr}}]$. For $h \to 0$ the jump $[u_h^{\mathrm{corr}}]$ vanishes and the discrete flux $\vec{j}_h^{\mathrm{corr}}$ converges to the flux $\vec{j}^{\mathrm{corr}}$ as defined in (2.6). □

3. Methods.

3.1. Implementation and parameter settings. We implemented the DG-FEM subtraction approach in the DUNE framework [8, 7] using the DUNE PDELab toolbox [11]. For reasons of comparison, we also implemented the CG-FEM subtraction approach in the same framework. We use linear ansatz functions for both DG (i.e., $k = 1$ in (2.12)) and CG approach throughout this study. On a given triangulation $\mathcal{T}_h$ we choose basis functions $\{\phi_h^i\}$, $i \in [0, N_h)$ with local support, where N_h denotes the number of unknowns. For the CG simulations a Lagrange basis with the usual hat functions is employed, whereas for the DG case element-wise L^2-orthonormal functions are chosen. In this setup ($k = 1$, hexahedral mesh), we have eight unknowns per mesh cell for the DG approach, i.e., $N_h = 8 \times \#\text{cells}$, and we have one unknown per vertex for the CG appraoch, i.e., $N_h = \#\text{vertices}$. Evaluating the bilinear forms $a(\cdot,\cdot)$, $J(\cdot,\cdot)$ and the right hand side $l(\cdot)$ leads to a linear system $A \cdot x = b$, where $x \in \mathbb{R}^{N_h}$ denotes the coefficient vector and the approximated solution of (2.24) is $u_h^{corr} = \sum_i x_i \phi_h^i$. Furthermore $A \in \mathbb{R}^{N_h \times N_h}$ is the matrix representation of the bi-linear operator $a + J$ and $b \in \mathbb{R}^{N_h}$ the right hand side vector:

$$
\begin{aligned}
A_{ij} &= a(\phi_h^j, \phi_h^i) + J(\phi_h^j, \phi_h^i) && i, j \in [0, N_h) \\
b_i &= l(\phi_h^i) && i \in [0, N_h)\,.
\end{aligned}
$$

TABLE 3.1
Conductive compartments (from in- to outside)

Compartment	Outer Radius	Conductivity
Brain	78 mm	0.33 S/m
CSF	80 mm	1.79 S/m
Skull	86 mm	0.01 S/m
Skin	92 mm	0.43 S/m

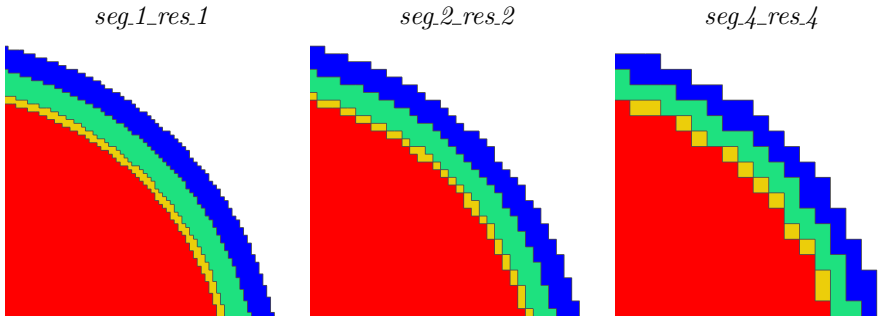

FIG. 3.1. *Visualization of models seg_1_res_1, seg_2_res_2 and seg_4_res_4 (from left to right), cut in x-plane at the origin; coloring is brain - red, CSF - yellow, skull - green, skin - blue.*

The resulting matrix A has sparse block structure with small dense blocks, in our case 8×8 matrices. The outer structure is similar to that of a finite volume discretization, i.e., rows corresponding to each grid cell and one off-diagonal entry for each cell neighbour. By now, a range of efficient solvers for DG discretizations is available, using techniques like Multigrid methods [9] or Domain Decomposition methods [2].

3.2. Volume conductor models. To validate and compare the accuracy of these numerical schemes, we used four layer sphere volume conductor models, where an analytical solution exists and can be used as reference [20]. For the four spherical compartments representing brain, cerebrospinal fluid (CSF), skull and skin we chose radii and conductivities as shown in Table 3.1. As motivated in the introduction and in 2.3, we used hexahedral meshes in our study. To be able to distinguish between numerical and geometrical errors, we constructed a variety of head models with different geometry/segmentation accuracies (1 mm, 2 mm and 4 mm) and for each of these we again used different mesh resolutions (1 mm, 2 mm and 4 mm). The details of these head models are listed in Table 3.2 and Figure 3.1 visualizes a subset of the used models.

To further evaluate the sensitivity of the different numerical methods to leakage effects, we intentionally generated spherical models with skull leakages. Therefore, we chose the model *seg_2_res_2* and reduced the radius of the outer skull boundary to 82 mm, 83 mm and 84 mm, resulting in skull thicknesses of 2 mm, 3 mm and 4 mm, respectively. Thereby we were able to generate a leakage scenario similar to the one presented in Figure 2.1, while preserving the advantage of a spherical solution that can be used for error evaluations. Table 3.3 indicates the number of leaks for each model, i.e., the number of vertices belonging to both an element labeled as skin and an element labeled as CSF or brain.

TABLE 3.2
Model parameters

	Seg.	Res.	#nodes	#elements
seg_1_res_1	1 mm	1 mm	3,342,701	3,262,312
seg_2_res_1	2 mm	1 mm	3,343,801	3,263,232
seg_2_res_2	2 mm	2 mm	428,185	407,907
seg_4_res_1	4 mm	1 mm	3,351,081	3,270,656
seg_4_res_2	4 mm	2 mm	429,077	408,832
seg_4_res_4	4 mm	4 mm	56,235	51,104

TABLE 3.3
Model parameters

	out. Skull Rad.	#leaks
seg_2_res_2_r82	82 mm	10,080
seg_2_res_2_r83	83 mm	1,344
seg_2_res_2_r84	84 mm	0

3.3. Sources. We used 10 different source eccentricities and, for each eccentricity, randomly distributed 10 sources to gain an overview of the range of the numerical accuracy, since it might depend on the local mesh structure. We evaluated the accuracy for both radial and tangential dipole directions, however, we only present the results for radial directions here. The results for dipoles with tangential direction are very similar with slightly higher overall errors for the radial dipoles.

To make the effect of skull leakage better accessible, we furthermore generated visualizations of the current for one dipole fixed at position $(1, 47, 47)$, which corresponds to an element center, and fixed direction $(0, 1, 1)$ for both CG- and DG-FEM and for all three models with reduced skull thickness as shown in Table 3.3. We visualized a cut through the x-plane at the dipole position and chose to visualize both the direction and strength of the electric flux for each numerical method and model (Fig. 4.4) and the relative change in strength and the flux difference between the numerical methods, described by the metrics $lnMAG_{\vec{j},loc}$ and $totDIFF_{\vec{j},loc}$ as defined in the next section, in each model (Fig. 4.5).

3.4. Error metrics. To achieve a result that purely represents the numerical and geometrical accuracy and is independent of the chosen sensor configuration, we evaluated the solutions on the whole outer layer. We use two different error measures to distinguish between topography and magnitude errors, the relative difference measure (RDM)

$$RDM(u_h, u) = \left\| \frac{u_h}{\|u_h\|_2} - \frac{u}{\|u\|_2} \right\|_2 \tag{3.1}$$

and the logarithmic magnitude error (lnMAG)

$$lnMAG(u_h, u) = \ln\left(\frac{\|u_h\|_2}{\|u\|_2} \right). \tag{3.2}$$

Besides presenting the mean RDM and lnMAG errors over all sources at a certain eccentricity (see, e.g., left subfigures in Fig. 4.1), we also present results in separate boxplots (see, e.g., right subfigures in Fig. 4.1). The boxplots show maximum and minimum, indicated by upper and lower error bars, and thereby the total error range. Furthermore, it includes the interval between upper and lower quartile, i.e., the interquartile range, also knows as the spread, which is marked by a box with a black dash showing the median. Note the different presentation of source eccentricity on the x-axes in the left and right subfigures.

To evaluate the local changes of the current, we furthermore visualize for each mesh element E the logarithm of the local change in current magnitude

$$lnMAG_{\vec{j},loc}(E) = \ln\left(\frac{\|\vec{j}_{h,\mathrm{CG}}(x_E)\|_2}{\|\vec{j}_{h,\mathrm{DG}}(x_E)\|_2}\right), \tag{3.3}$$

and the total local current difference

$$totDIFF_{\vec{j},loc}(E) = \vec{j}_{h,\mathrm{CG}}(x_E) - \vec{j}_{h,\mathrm{DG}}(x_E), \tag{3.4}$$

where x_E denotes the centroid of mesh element E (see Fig. 4.5).

For both the classical lnMAG and the $lnMAG_{\vec{j},loc}$, we can exploit that due to the relation $\ln(1+x) \approx x$ for small $\|x\|$, we have $lnMAG \approx \|u_h\|_2/\|u\|_2 - 1$ for small deviations and $100 \cdot lnMAG$ is about the change of the magnitude in percent and accordingly for the $lnMAG_{\vec{j},loc}$.

4. Results. Figure 4.1 shows the convergence of RDM and lnMAG errors for the DG method when increasing the geometrical accuracy. Comparing the results for meshes *seg_1_res_1*, *seg_2_res_2* and *seg_4_res_4* shows the clear reduction of both RDM and lnMAG when increasing the mesh resolution and improving the representation of the geometry at the same time. The finest mesh *seg_1_res_1* achieves accuracies below 0.05 with regard to the RDM for eccentricities up to 0.979, i.e., a distance of 1.6 mm to the brain/CSF boundary. For an eccentricity of 0.987, i.e., a distance of about 1 mm to the brain/CSF boundary, this error increases up to maximally 0.1. For even higher eccentricities the errors clearly increase up to values of 0.5 maximally. However, the median error stays clearly below 0.2 here and minimal errors are still at about 0.05. The behaviour with regard to the lnMAG is very similar, being nearly constant up to an eccentricity of 0.979, slightly increasing for an eccentricity of 0.987 and strongly increasing with a high error range for higher eccentricities. The errors for meshes *seg_2_res_2* and *seg_4_res_4* are clearly higher than for mesh *seg_1_res_1*. However, additionally displaying the results for the refined meshes *seg_2_res_1*, *seg_4_res_1* and *seg_4_res_2*, where the geometry error is kept constant, allows us to estimate whether the increased errors are due to insufficient numerical accuracy or the inaccurate resolution of the geometry. We find that for both a geometry resolution of 2 mm and 4 mm the errors are dominated by the geometry error. Comparing the models with a geometry resolution of 2 mm, we find nearly identical errors with regard to the RDM up to an eccentricity of 0.964 (see right subfigure in Fig. 4.1). Here, the median of the error stays below 0.1. For higher eccentricities, where sources are already placed in the outermost layer of elements that still belong to the brain compartment, the errors for the lower resolved mesh increase clearly faster; especially for the two highest eccentricities the differences are large. With regard to the lnMAG, even for the outermost sources the effect of the higher mesh resolution is clearly weaker, notable differences can only be seen due to some outliers, while the median errors stay in a

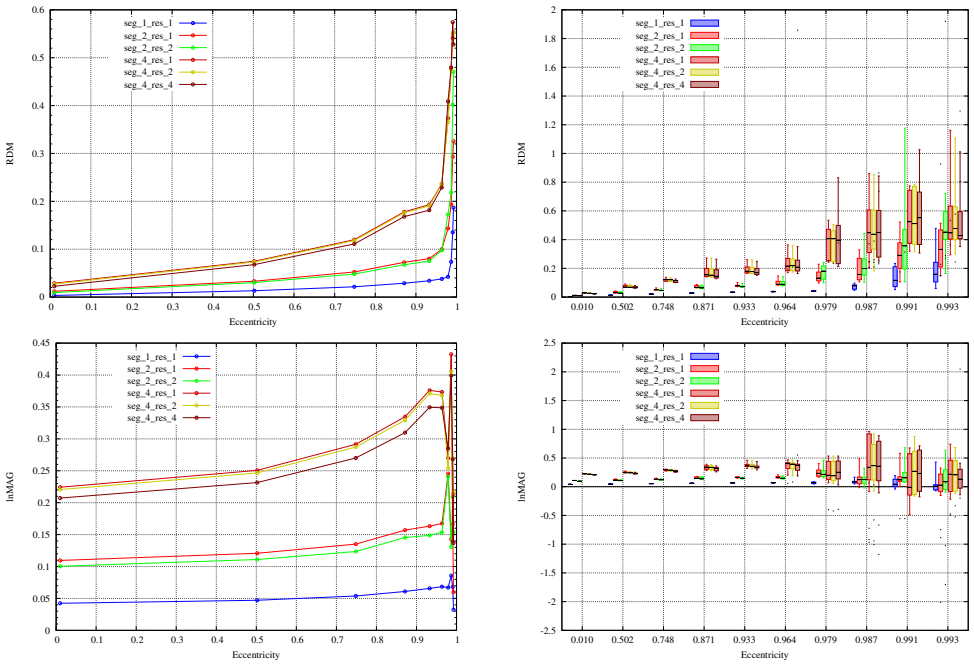

FIG. 4.1. *Convergence for DG-FEM with increasing mesh and/or geometrical resolution. Results of radial dipole computations. Visualized are the mean error (left column) and boxplots (right column) of RDM (top row) and lnMAG (bottom row). Dipole positions that are outside the brain compartment in the discretized models are marked as dots. Note the different scaling of the x-axes.*

similar range for both resolutions. For the meshes with a geometry resolution of 4 mm, only negligible differences can be seen at all eccentricities; the medians of the errors are very similar, differences can only be found in the maximal values but do not show a systematic behaviour. However, the errors are clearly increased compared to the models with a better approximation of the geometry: Already at an eccentricity of about 0.5 the median RDM is at about 0.1, increasing to values above 0.4 for the highest four eccentricities. The same behaviour is observed for the lnMAG, again finding significantly increased errors compared to the models with a more accurate representation of the geometry.

In Figure 4.2 the results for the newly proposed DG-FEM are presented side by side to the CG-FEM for the meshes *seg_1_res_1*, *seg_2_res_2* and *seg_4_res_4*. For the model *seg_1_res_1* the only notable difference with regard to the RDM can be observed for the highest eccentricity, where the DG-FEM achieves slightly higher accuracies; the evaluation of the lnMAG shows even less differences. Also for model *seg_2_res_2* the two approaches achieve a very similar numerical accuracy for the lower eccentricities with RDM errors clearly below 0.1; for eccentricities between 0.964 and 0.991 the CG-FEM performs slightly better, while for the highest eccentricity the DG-FEM achieves a higher accuracy, again. However, as analyzed before, also here the main error source is the inaccurate representation of the geometry. The lnMAG shows no systematic difference in accuracy between the two methods in this model. In the coarsest model, *seg_4_res_4*, the DG-FEM performs clearly better than CG-FEM already for low eccentricities. Regardless of the high geometry errors, as also already observed in Figure 4.1, larger differences in numerical accuracy between DG- and

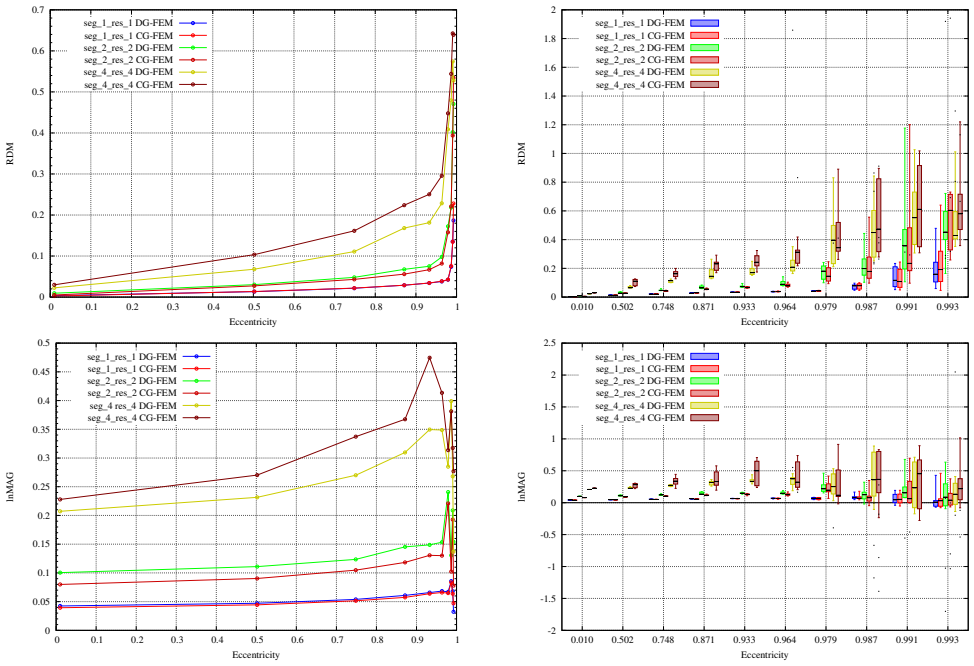

FIG. 4.2. *Convergence for both CG-FEM and DG-FEM with increasing mesh and geometrical resolution. Results of radial dipole computations. Visualized are the mean error (left column) and boxplots (right column) of RDM (top row) and lnMAG (bottom row). Dipole positions that are outside the brain compartment in the discretized models are marked as dots. Note the different scaling of the x-axes.*

CG-FEM can be observed for both RDM and lnMAG up to an eccentricity of 0.964. For higher eccentricities, possible differences can be less clearly distinguished due to the dominance of the geometry error and the resulting generally increased error level.

The most significant accuracy differences between DG- and CG-FEM can be seen in Figure 4.3 where we study the increase of errors for decreasing skull thickness and resulting increase in the number of skull leakages (see Table 3.3). While we still find a very similar numerical accuracy for DG- and CG-FEM in the leakage-free model *seg_2_res_2_r84* (4 mm skull thickness), as one would expect given the previous results, the DG-FEM performs clearly better in the leaky models *seg_2_res_2_r82* (2 mm skull thickness) and *seg_2_res_2_r83* (3 mm skull thickness). Already for low eccentricities the sensitivity of the CG-FEM to leakages is distinct. The DG-FEM achieves an only slightly decreased accuracy in the model *seg_2_res_2_r83* compared to *seg_2_res_2_r84*, which already shows that this approach is clearly less sensitive to leakages. In contrast, the errors of the CG-FEM for model *seg_2_res_2_r83* are much higher than for model *seg_2_res_2_r84* (compare *seg_2_res_2_r83 CG-FEM* with *seg_2_res_2_r84 CG-FEM*) and already in the range of those of the DG-FEM in the very leaky model *seg_2_res_2_r82* (compare *seg_2_res_2_r83 CG-FEM* with *seg_2_res_2_r82 DG-FEM*). Overall, we find that the DG-FEM achieves a significantly higher numerical accuracy than the CG-FEM already for low eccentricities in the leaky models, both with regard to RDM and lnMAG.

To illustrate the effect of skull leakage, we generated the visualizations shown in Figures 4.4 and 4.5. In Figure 4.4, the electric current direction and strength for a

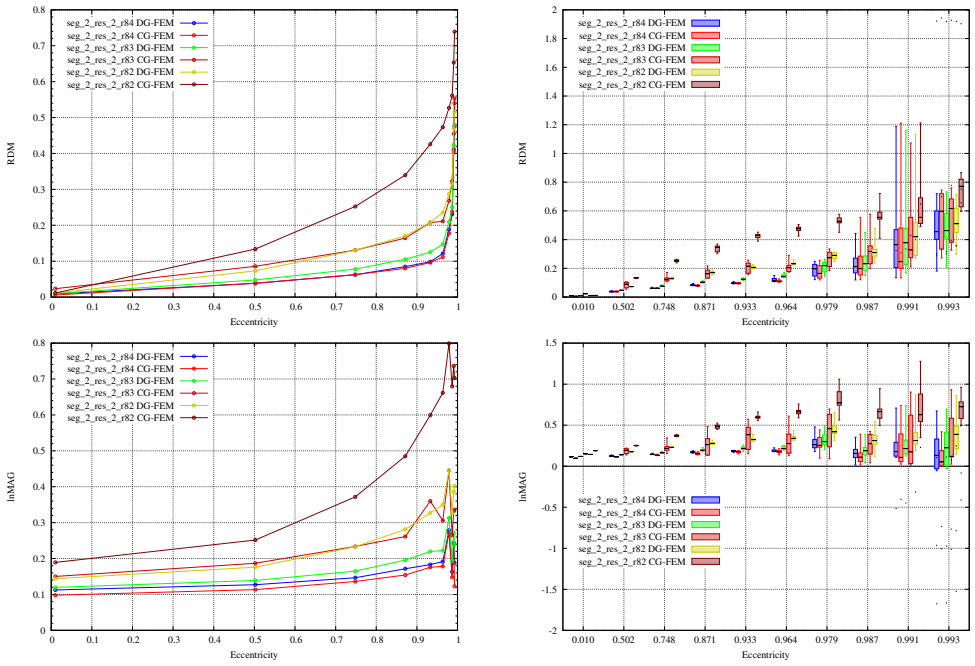

FIG. 4.3. *Comparison of increase of errors for decreasing skull thickness between CG-FEM and DG-FEM. Results of radial dipole computations. Visualized are the mean error (left column) and boxplots (right column) of RDM (top row) and lnMAG (bottom row). Dipole positions that are outside the brain compartment in the discretized models are marked as dots. Note the different scaling of the x-axes.*

radial dipole with fixed position and orientation (turquoise cone in the middle and right columns) in the models *seg_2_res_2_r82* (top row), *seg_2_res_2_r83* (middle row), and *seg_2_res_2_r84* (bottom row) and with the two numerical approaches CG-FEM (middle column) and DG-FEM (right column) is visualized. When using CG-FEM in the model with the thinnest (2 mm) skull compartment, *seg_2_res_2_r82*, we find extremly strong currents in the innermost layer of skin elements, i.e., at the interface to the skull. This is especially distinct for those elements the dipole is nearly directly pointing to. In comparison, the current strengths found in the skull compartment are negligible, which is a clear sign for a current leakage through the vertices shared between CSF and skin compartment, bypassing the thin and leaky skull compartment. For the DG approach, these extreme peaks are not found and the maximal current strength amounts to only about 30% of that of the CG approach. In the other two models (note the much lower scaling in the middle and lower rows in Figure 4.4) we find a clear decrease of the current strength in the skin compartment compared to the *seg_2_res_2_r82* model. In these two models and with the given source scenario, none of the approaches seems to be obviously affected by skull leakage. While in model *seg_2_res_2_r83* (middle row) the DG approach shows about 20% higher peak currents in the innermost layer of skin elements compared to CG-FEM, the maximal current strength for the CG-FEM is about 7% higher than for the DG-FEM and found in the skull compartment in model *seg_2_res_2_r84* (bottom row). These deviations seem reasonable considering the relatively coarse representation of the geometry. The visualizations show that the interplay between source position and direction and the

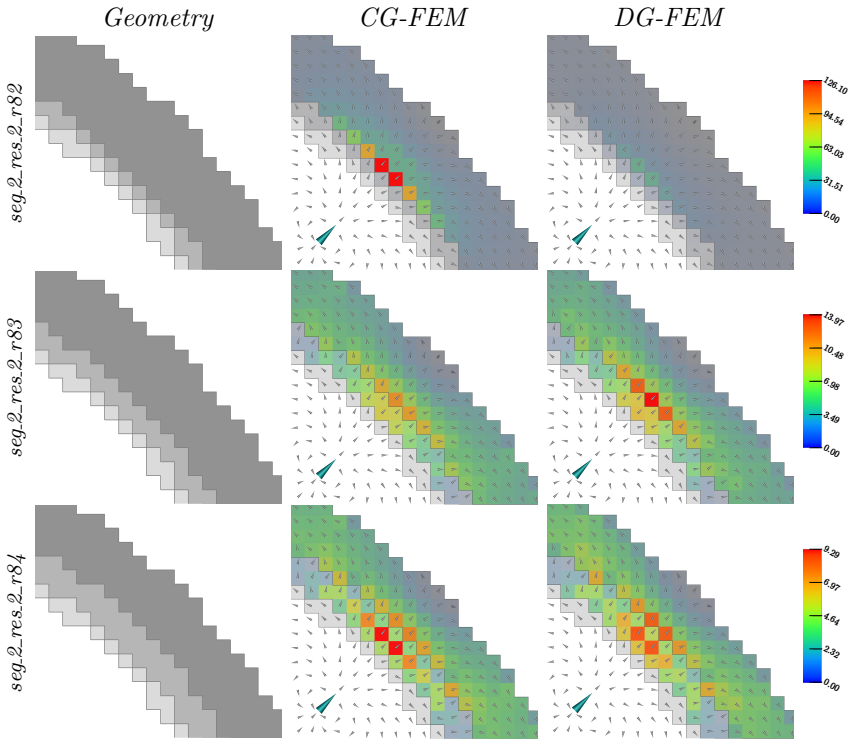

FIG. 4.4. *Visualization of model geometry (left column), current direction and strength for CG-FEM (middle column) and DG-FEM (right column) for models seg_2_res_2_r82 (top row), seg_2_res_2_r83 (middle row), and seg_2_res_2_r84 (bottom row). The left column shows the model geometry, interior to exterior from bottom left to top right, brain in white, CSF, skull and skin in increasingly dark grey, and air in white. Dark grey lines mark compartment boundaries. In the middle and right columns, the large turquoise cone presents the dipole source. The small and normalized grey cones show the directions of the current flow and, for elements belonging to skull and skin compartments, the coloring indicates the current strength. For each model the color scale is kept constant for both approaches.*

local geometry strongly influences the local current flow in these models, leading to current peaks in some elements while neighbouring elements show relatively low currents, as it is clearly visible in model *seg_2_res_2_r84*. In this model we find strong currents in the two skull elements the dipole is pointing to and that are providing a "shortcut" between CSF and skin compartment and thereby the lowest resistance.

In Figure 4.5 the two measures $lnMAG_{\vec{j},loc}$ and $totDIFF_{\vec{j},loc}$ are visualized to show the differences between the two methods even more clearly. As Figure 4.4 already suggests, we find for model *seg_2_res_2_r82* that for the CG-FEM the current strength is clearly higher than for the DG-FEM in those elements of the innermost layer of the skin compartment that share a vertex with the CSF compartment, indicated by the high $lnMAG_{\vec{j},loc}$ (red coloring). The visualization of the $totDIFF_{\vec{j},loc}$ (grey arrows) clearly shows that the leakage generates a strong current from the CSF compartment directly into the skin compartment that is not existing for the DG-FEM. At the same time the current in the skull compartment is decreased in the CG-FEM; the visualization (see Fig. 4.4 and zoom into Figure 4.5) of the $totDIFF_{\vec{j},loc}$ shows that there is actually a stronger current through the skull elements in the DG-FEM simulation (inwards pointing arrows). We also find high values for the $totDIFF_{\vec{j},loc}$ in the CSF

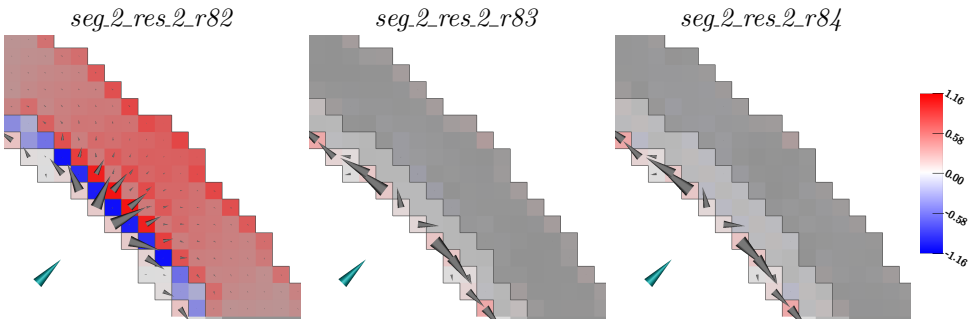

FIG. 4.5. *Visualization of current flow differences between CG- and DG-FEM in models seg_2_res_2_r82 (left), seg_2_res_2_r83 (middle), and seg_2_res_2_r84 (right). The turquoise cone presents the dipole source. The coloring shows the* $lnMAG_{\vec{j},loc}$ *(increase/decrease of the current strength simulated with the CG- compared to the DG-FEM solution). For all models the maximum of the color scale is chosen as the maximal value in the skin and skull compartment. Grey cones, having the same linear scaling for all models, show the* $totDIFF_{\vec{j},loc}$ *(difference in current flow). In models seg_2_res_2_r83 and seg_2_res_2_r84 the arrows in skin and skull are not visible due to the relatively small values. Dark grey lines mark compartment boundaries.*

compartment, which are most probably caused by effects similar to the "leakage" effects, i.e., a mixing of conductivities in boundary elements/vertices. However, in model *seg_2_res_2_r82*, the color-coding for the $lnMAG_{\vec{j},loc}$ shows that this is not related to significant relative differences in current strength. Here, the strongest values for the $lnMAG_{\vec{j},loc}$ are found in the skin and skull compartment. In turn, for the other two models we find the largest deviations in the CSF compartment, both with regard to $totDIFF_{\vec{j},loc}$ and $lnMAG_{\vec{j},loc}$. For model *seg_2_res_2_r83* we furthermore find minor effects in $lnMAG_{\vec{j},loc}$, i.e., relative differences of current strength, in the innermost layer of skin elements, which are also the elements with the highest absolute current strength among skin and skull compartment (see also Fig. 4.4). We also find slightly increased values for the $lnMAG_{\vec{j},loc}$ in the outermost layer of skin elements. These might be artifacts due to the "staircase"-like geometry of the outer surface in the regular hexahedral model. However, the $totDIFF_{\vec{j},loc}$ in skin and skull is negligible compared to the CSF compartment. The same holds true for model *seg_2_res_2_r84*, where $lnMAG_{\vec{j},loc}$ is slightly increased in skull and skin compartment mainly in elements with a small absolute current strength, as a comparison to Figure 4.4 shows. Still, relatively high differences in $lnMAG_{\vec{j},loc}$ and $totDIFF_{\vec{j},loc}$ are visible in the CSF compartment. These results indicate that model *seg_2_res_2_r83* and *seg_2_res_2_r84* are less affected by skull-leakage, the differences are rather due to the different computational approaches and do not show obvious errors due to the model geometry.

5. Discussion. In this paper we presented the theoretical derivation of the subtraction FE approach for EEG forward simulations in the framework of Discontinuous Galerkin methods. The scheme is consistent and fulfils a discrete conservation property. Existence and uniqueness follow from the coercivity of the bilinear form.

The numerical experiments showed the convergence of the DG solution towards the analytical solution with increasing mesh resolution and better approximation of the spherical geometry. We could furthermore show that the numerical accuracy of the DG-FEM is dominated by the geometry error, while the actual mesh resolution in a model with bad geometry approximation only had a minor influence on the numerical

results (Fig. 4.1). The inaccurate representation of the geometry, especially in the coarser meshes, is visible by the "staircase-like" boundaries in Figure 3.1.

In the comparisons of DG- and the commonly used CG-FEM, we did not find remarkable differences for meshes with higher resolutions (1 mm, 2 mm), as the results in Figure 4.2 are in the same range for both approaches in the models *seg_1_res_1* and *seg_2_res_2*. In this set of experiments, three main error sources can be identified, namely geometry errors, numerical inaccuracies, and leakage effects:

First, there is the error in the representation of the geometry, which is especially strong in the models with low resolution, see also Figure 4.1. We thus strongly recommend to use geometry resolutions, and thereby necessarily MRI resolutions, as high as practically feasible, possibly even locally-refined when zoomed MRI technology is available. In fact, since recently a newly developed zoom technique for MRI is available for practical use, based on a combination of parallel transmission of excitation pulses and localized excitation [14]. A first usage of this zoom technique can be found in [4, Chapter 5]. Moreover, in future work, based on [10], we plan to further develop a cut-cell approach that allows for an accurate representation of the geometry while only introducing a negligible amount of additional degrees of freedom. Thus, the achieved accuracy can be increased while the computational effort is hardly affected (see first results in [34]).

Second, we have the numerical inaccuracy due to the discretization of Equation (2.1) in combination with the strong singularity introduced by the assumption of a point dipole. This is the main cause for the numerical inaccuracies of the subtraction approach for highest eccentricities, where the source positions are very close to the next conductivity jump (cf. Fig.4.2). A rational for this effect has been given in [59, 23]. In future work, we are therefore planning to adapt other source modeling approaches like the Venant [47, 43, 17, 58, 51], the partial integration [60, 53, 58, 48, 51] or the Whitney approach [46, 35] to the DG-FEM framework, that have until now only been formulated and evaluated for CG-FEM. Compared to the subtraction approach, these approaches have the further advantage of a strongly decreased computational effort for the setup of the right-hand-side vector [58, 51].

The third source of error, the "leakage effects", explain the large differences in numerical accuracy between CG- and DG-FEM that can be observed in model *seg_4_res_4*. Due to the coarse resolution in comparison to the thickness of the skull compartment (4 mm resolution, 6 mm thickness), this model can already be considered as (at least partly) leaky.

This observation motivated the evaluation of the two methods in a scenario where the ex ante assumed advantages of the DG-FEM would have a bigger effect. Therefore, we constructed spherical models with a thinner skull layer, finally ending up with the model *seg_2_res_2_r82* that has a skull layer as thin as the edge length of the hexahedrons (see Figs. 4.3, 4.4, 4.5). Even if 1 mm FEM resolution is strongly recommended for practical application of source analysis [38, 6, 5], 2 mm FEM resolution is still used even in clinical evaluations [13], and there are areas such as the temporal bone, where skull thickness is 2 mm or even less [30, Table 2], so that this is not an artificial scenario. As expected, the DG-FEM achieved a clearly higher numerical accuracy in the two models with the thinnest skull layers, *seg_2_res_2_r82* and *seg_2_res_2_r83*, while the results for model *seg_2_res_2_r84* are comparable for DG- and CG-FEM (see Fig. 4.3). In the latter model, the ratio of resolution (2 mm) and skull thickness (4 mm) guarantees sufficient resolution and by this already prohibits leakages.

To make the difference between CG- and DG-FEM in the presence of skull leakage better accessible, we generated Figures 4.4 and 4.5. The skull leakage is clearly visible in both figures for model *seg_2_res_2_r82* and the CG-FEM as described in the results section. There is also a slight difference visible in the CSF in all three models, which might be explained by the relatively thin CSF layer. In this resolution (2 mm thickness, 2 mm segmentation/mesh resolution) the elements of the CSF compartment are no longer completely connected via faces, but often only via shared vertices (as visible in Fig. 4.4 (left column)). This means that for such a coarse model, the current is blocked in some regions, although in the real geometry it isn't. In this case the CG-FEM shows slightly better results, as it allows the current to also flow through a single vertex, which is physically counterintuitive. In contrast the DG-FEM does exactly, what one would intuitively expect from this particular geometry, it channels the main current through the CSF, but due to the wrong representation of the CSF it yields slightly wrong currents. It thereby reduces the usually very strong current in the highly-conductive CSF compartment. This might explain the slight advantages of the CG-FEM with regard to numerical accuracy for model *seg_2_res_2_r84* (see especially lnMAG in Fig. 4.3, which is in agreement with the strong lnMAG effect of CSF as shown in [50, Fig.4]). Still one has to point out that these geometric errors in the CSF only have a very minor effect, as they don't block the current completely, but only divert it slighty.

Overall, these results show benefits of the newly derived DG-FEM approach and motivate the introduction of this new numerical approach for solving the EEG forward problem. Furthermore, the DG-FEM approach allows for an intuitive interpretation of the results, in the presence of geometric artifacts. This helps in the interpretation of simulation results in particular for clinical experts.

As we have shown in this study, errors in the approximation of the geometry and resulting current leakages might become significant sources of error when using regular hexahedral meshes with coarse resolutions. However, there are possibilities to avoid such errors. In [48], a trilinear immersed finite element method to solve the EEG forward problem was introduced, which allows to use structured hexahedral meshes, i.e., the mesh structure is independent of the physical boundaries. The interfaces are then represented by level-sets and finally considered using special basis functions. However, this method is still based on the CG-FEM formulation, so that the behaviour when the thickness of single compartments lies in the range of the resolution of the underlying mesh is unclear, especially when both the compartment boundaries between CSF and skull (inner skull surface) and skull and skin (outer skull surface) are contained in one element; it is probable that it suffers from the same problems as the common CG-FEM in such cases. Unfortunately, no further in-depth analysis for this approach was performed until now. Therefore, we claim to have for the first time presented and evaluated a FEM approach preventing current leakage through single nodes. In future investigations, we intend to further develop the already discussed cut-cell DG approach for source analysis [34], which has the same advantageous features with regard to the representation of the geometry as the approach presented in [48], but additionally the charge preserving property of the DG-FEM as presented here.

The charge preserving property could also be achieved by certain implementations of finite volume methods. In [19], a vertex-centered finite volume approach was presented, which shares the advantage with the here presented DG-FEM approaches that anisotropic conductivities can be treated quite naturally. However, due to its

construction, the vertex-centered approach can also be affected by unphysical current flow between high-conducting compartments that touch in single nodes as seen for the CG-FEM. This problem could be avoided using a cell-centered finite volume approach.

Computational costs were not explicitly evaluated in this paper. Obviously, due to the more complex structure (see equation (2.24)), the setup of the stiffness matrix and the iterative solving is more time-consuming for DG- than for CG-FEM. Moreover, as for all FEM-based approaches in source analysis, the number of equation systems that have to be solved can be limited to the number of sensors by the implementation of transfer matrices so that this computationally more expensive part has to be performed only once per head model and sensor arrangement [53, 25, 57, 35].

Finally, since the DG approach allows to fulfill the conservation property of electric charge also in the discrete case, it is not only attractive for source analysis, but also for the optimization of brain stimulation methods like transcranial direct or alternating current stimulation (tCS, tDCS, tACS) [22, 40, 56, 34, 52] or deep brain stimulation [18, 42].

6. Conclusion. We presented theory and numerical evaluation of the subtraction finite element method (FEM) approach for EEG forward simulations in the Discontinuous Galerkin framework (DG-FEM). We evaluated the accuracy and convergence of the newly presented approach in spherical models for different mesh resolutions and compared it to the frequently used Lagrange- or Continuous Galerkin- (CG-) FEM. Here, we found similar accuracies of the two approaches for high mesh resolutions, while the DG- outperformed the CG-FEM for low mesh resolutions. We further compared the approaches in the special scenario of a very thin skull layer, where "leakages" might occur. We found that the DG approach clearly outperforms CG-FEM in these scenarios. We underlined these results using visualizations of the electric current flow. The DG-FEM approach might therefore complement CG-FEM for improving source analysis approaches.

REFERENCES

[1] Z. Akalin Acar and S. Makeig, *Neuroelectromagnetic forward head modeling toolbox*, Journal of Neuroscience Methods, 190 (2010), pp. 258–270.

[2] P. F. Antonietti and P. Houston, *A class of domain decomposition preconditioners for hp-discontinuous galerkin finite element methods*, Journal of Scientific Computing, 46 (2011), pp. 124–149.

[3] D. N. Arnold, F. Brezzi, B. Cockburn, and L. D. Marini, *Unified Analysis of Discontinuous Galerkin Methods for Elliptic Problems*, SIAM Journal on Numerical Analysis, 39 (2002), pp. 1749–1779.

[4] Ümit Aydin, *Combined EEG and MEG source analysis of epileptiform activity using calibrated realistic finite element head models*, PhD thesis, PhD thesis, Fakultät für Informatik und Automatisierung, 2015.

[5] Ü. Aydin, J. Vorwerk, M. Dümpelmann, P. Küpper, H. Kugel, M. Heers, J. Wellmer, C. Kellinghaus, J. Haueisen, S. Rampp, H. Stefan, and C. H. Wolters, *Combined eeg/meg can outperform single modality eeg or meg source reconstruction in presurgical epilepsy diagnosis*, PLoS ONE, 10 (2015), p. e0118753. doi: 10.1371/journal.pone.0118753.

[6] Ü. Aydin, J. Vorwerk, P. Küpper, M. Heers, H. Kugel, A. Galka, L. Hamid, J. Wellmer, C. Kellinghaus, S. Rampp, S. Hermann, and C. H. Wolters, *Combining EEG and MEG for the reconstruction of epileptic activity using a calibrated realistic volume conductor model*, PloS ONE, 9 (2014), p. e93154.

[7] P. Bastian, M. Blatt, A. Dedner, C. Engwer, R. Klöfkorn, R. Kornhuber, M. Ohlberger, and O. Sander, *A generic grid interface for parallel and adaptive scientific computing. Part II: Implementation and tests in DUNE*, Computing, 82 (2008), pp. 121–138.

[8] P. Bastian, M. Blatt, A. Dedner, C. Engwer, R. Klöfkorn, M. Ohlberger, and O. Sander, *A generic grid interface for parallel and adaptive scientific computing. Part I: Abstract framework*, Computing, 82 (2008), pp. 103–119.

[9] P. Bastian, M. Blatt, and R. Scheichl, *Algebraic multigrid for discontinuous galerkin discretizations of heterogeneous elliptic problems*, Numerical Linear Algebra with Applications, 19 (2012), pp. 367–388.

[10] P. Bastian and C. Engwer, *An unfitted finite element method using discontinuous Galerkin*, International Journal for Numerical Methods in Engineering, 79 (2009), pp. 1557–1576.

[11] P. Bastian, F. Heimann, and S. Marnach, *Generic implementation of finite element methods in the distributed and unified numerics environment (DUNE)*, Kybernetika, 46 (2010), pp. 294–315.

[12] O. Bertrand, M. Thévenet, and F. Perrin, *3D finite element method in brain electrical activity studies*, in Biomagnetic Localization and 3D Modelling, J. Nenonen, H.M. Rajala, and T. Katila, eds., Report of the Department of Technical Physics, Helsinki University of Technology, 1991, pp. 154–171.

[13] G. Birot, L. Spinelli, S. Vulliemoz, P. Megevand, D. Brunet, M. Seeck, and C.M. Michel, *Head model and electrical source imaging: A study of 38 epileptic patients.*, NeuroImage: Clinical, 5 (2014), pp. 77–83.

[14] M. Blasche, P. Riffel, and M. Lichy, *Timtx trueshape and syngo zoomit technical and practical aspects.*, Magnetom Flash, 1 (2012), pp. 74–84.

[15] D. Braess, *Finite Elements: Theory, Fast Solvers, and Applications in Solid Mechanics*, Springer, 2007.

[16] R. Brette and A. Destexhe, *Handbook of Neural Activity Measurement*, Cambridge University Press, ISBN 978-0-521-51622-8, 2012. doi: 10.1017/CBO9780511979958.

[17] H. Buchner, G. Knoll, M. Fuchs, A. Rienäcker, R. Beckmann, M. Wagner, J. Silny, and J. Pesch, *Inverse localization of electric dipole current sources in finite element models of the human head*, Electroencephalography and Clinical Neurophysiology, 102 (1997), pp. 267–278.

[18] C.R. Butson, S.E. Cooper, J.M. Henderson, and C.C. McIntyre, *Patient-specific analysis of the volume of tissue activated during deep brain stimulation.*, NeuroImage, 34 (2007), pp. 661–670.

[19] M. J. D. Cook and Z. J. Koles, *A high-resolution anisotropic finite-volume head model for EEG source analysis*, in Proceedings of the 28th Annual International Conference of the IEEE Engineering in Medicine and Biology Society, 2006, pp. 4536–4539.

[20] J. C. de Munck and M. Peters, *A fast method to compute the potential in the multi sphere model*, IEEE Transactions on Biomedical Engineering, 40 (1993), pp. 1166–1174.

[21] D. A. Di Pietro and A. Ern, *Mathematical Aspects of Discontinuous Galerkin Methods*, vol. 69, Springer, 2011.

[22] J.P. Dmochowski, A. Datta, M. Bikson, Y. Su, and L.C. Parra, *Optimized multi-electrode stimulation increases focality and intensity at target.*, J. Neural Eng., 8 (2011), p. 046011 (16pp).

[23] F. Drechsler, C. H. Wolters, T. Dierkes, H. Si, and L. Grasedyck, *A full subtraction approach for finite element method based source analysis using constrained delaunay tetrahedralisation*, NeuroImage, 46 (2009), pp. 1055–1065.

[24] A. Ern, A. F. Stephansen, and P. Zunino, *A discontinuous galerkin method with weighted averages for advection–diffusion equations with locally small and anisotropic diffusivity*, IMA Journal of Numerical Analysis, 29 (2009), pp. 235–256.

[25] N. G. Gencer and C. E. Acar, *Sensitivity of EEG and MEG measurements to tissue conductivity.*, Physics in Medicine and Biology, 49 (2004), pp. 701–717.

[26] S. Giani and P. Houston, *Anisotropic hp-adaptive discontinuous galerkin finite element methods for compressible fluid flows*, International Journal of Numerical Analysis and Modeling, 9 (2012), pp. 928–949.

[27] A. Gramfort, T. Papadopoulo, E. Olivi, and M. Clerc, *Forward field computation with OpenMEEG*, Computational Intelligence and Neuroscience, 2011 (2011), pp. 1–13. doi:10.1155/2011/923703.

[28] C. Grossmann, H.-G. Roos, and M. Stynes, *Numerical Treatment of Partial Differential Equations*, Springer, 2007.

[29] M. Hämäläinen, R. Hari, R. J. Ilmoniemi, J. Knuutila, and I. V. Lounasmaa, *Magnetoencephalographytheory, instrumentation, and applications to noninvasive studies of the working human brain*, Reviews of modern Physics, 65 (1993), p. 413.

[30] J.-H. Kwon, J.S. Kim, D.-W. Kang, K.-S. Bae, and S.U. Kwon, *The thickness and texture of temporal bone in brain ct predict acoustic window failure of transcranial doppler.*, J

Neuroimaging, 16 (2006), pp. 347–52.
[31] G. Marin, C. Guerin, S. Baillet, L. Garnero, and G. Meunier, *Influence of skull anisotropy for the forward and inverse problem in EEG: simulation studies using the FEM on realistic head models*, Human Brain Mapping, 6 (1998), pp. 250–269.
[32] V. Montes-Restrepo, P. van Mierlo, G. Strobbe, S. Staelens, S. Vandenberghe, and H. Hallez, *Influence of skull modeling approaches on eeg source localization*, Brain Topogr., 27 (2014), pp. 95–111.
[33] J. C. Mosher, R. M. Leahy, and P. S. Lewis, *EEG and MEG: Forward solutions for inverse methods*, IEEE Transactions on Biomedical Engineering, 46 (1999), pp. 245–259.
[34] A. Nüssing, C. H. Wolters, H. Brinck, and Engwer C., *The unfitted discontinuous galerkin method in brain research*, in International Conference on Basic and Clinical Multimodal Imaging (BaCI), 2015.
[35] S. Pursiainen, A. Sorrentino, C. Campi, and M. Piana, *Forward simulation and inverse dipole localization with the lowest order raviart-thomas elements for electroencephalography*, Inverse Problems, 27 (2011).
[36] C. Ramon, P. Schimpf, and J. Haueisen, *Influence of head models on EEG simulations and inverse source localizations*, BioMedical Engineering OnLine, 5 (2006).
[37] B. Rivière, M. F. Wheeler, and V. Girault, *A priori error estimates for finite element methods based on discontinuous approximation spaces for elliptic problems*, SIAM Journal on Numerical Analysis, (2002), pp. 902–931.
[38] M. Rullmann, A. Anwander, S. K. Dannhauer, M .and Warfield, F. H. Duffy, and C. H. Wolters, *EEG source analysis of epileptiform activity using a 1 mm anisotropic hexahedra finite element head model*, NeuroImage, 44 (2009), pp. 399–410.
[39] T. Papadopoulo S. Vallaghe and M. Clerc, *The adjoint method for general eeg and meg sensor-based lead field equations*, Physics in Medicine and Biology, 54 (2009), pp. 135–147.
[40] R.J. Sadleir, T.D. Vannorsdall, D.J. Schretlen, and B. Gordon, *Target optimization in transcranial direct current stimulation.*, Frontiers in Psychiatry, 3 (2012), pp. 1–13.
[41] P. H. Schimpf, C.R. Ramon, and J. Haueisen, *Dipole models for the EEG and MEG*, IEEE Transactions on Biomedical Engineering, 49 (2002), pp. 409–418.
[42] C. Schmidt, P. Grant, M. Lowery, and U. van Rienen, *Influence of uncertainties in the material properties of brain tissue on the probabilistic volume of tissue activated.*, IEEE Trans. Biomed. Eng., 60 (2013), pp. 1378–1387.
[43] R. Schönen, A. Rienäcker, R. Beckmann, and G. Knoll, *Dipolabbildung im FEM-Netz, Teil I*, Arbeitspapier zum Projekt Anatomische Abbildung elektrischer Aktivität des Zentralnervensystems, RWTH Aachen, Juli 1994.
[44] H. Sonntag, J. Vorwerk, C. H. Wolters, L. Grasedyck, J. Haueisen, and B. Maess, *Leakage effect in hexagonal FEM meshes of the EEG forward problem*, in International Conference on Basic and Clinical Multimodal Imaging (BaCI), 2013.
[45] M. Stenroos and J. Sarvas, *Bioelectromagnetic forward problem: isolated source approach revis(it)ed*, Physics in Medicine and Biology, 57 (2012), pp. 3517–3535.
[46] O. Tanzer, S. Järvenpää, J. Nenonen, and E. Somersalo, *Representation of bioelectric current sources using whitney elements in finite element method*, Physics in Medicine and Biology, 50 (2005), pp. 3023–3039.
[47] R. Toupin, *Saint-venants principle*, Archive for Rational Mechanics and Analysis, 18 (1965), pp. 83–96.
[48] S. Vallaghé and T. Papadopoulo, *A trilinear immersed finite element method for solving the electroencephalography forward problem*, SIAM Journal on Scientific Computing, 32 (2010), pp. 2379–2394.
[49] F. Vatta, F. Meneghini, F. Esposito, S. Mininel, and F. Di Salle, *Solving the forward problem in eeg source analysis by spherical and fdm head modeling: a comparative analysis*, Biomed Sci Instrum, 45 (2009), pp. 382–388.
[50] J. Vorwerk, J.-H. Cho, S. Rampp, H. Hamer, T. R. Knösche, and C. H. Wolters, *A guideline for head volume conductor modeling in EEG and MEG*, NeuroImage, 100 (2014), pp. 590 – 607.
[51] J. Vorwerk, M. Clerc, M. Burger, and C. H. Wolters, *Comparison of boundary element and finite element approaches to the eeg forward problem.*, Biomedizinische Technik. Biomedical engineering, 57 (2012).
[52] S. Wagner, S.M. Rampersad, Ü. Aydin, J. Vorwerk, T.F. Oostendorp, T. Neuling, C.S. Herrmann, D.F. Stegeman, and C.H. Wolters, *Investigation of tdcs volume conduction effects in a highly realistic head model*, J. Neural Eng., 11 (2014), p. 016002(14pp). doi: 10.1088/1741-2560/11/1/016002.
[53] D. Weinstein, L. Zhukov, and C. Johnson, *Lead-field bases for electroencephalography source*

imaging, Annals of Biomed.Eng., 28 (2000), pp. 1059–1066.

[54] K. Wendel, N. G. Narra, M. Hannula, P. Kauppinen, and J. Malmivuo, *The influence of CSF on EEG sensitivity distributions of multilayered head models.*, IEEE Transactions on Biomedical Engineering, 55 (2008), pp. 1454–1456.

[55] Mary Fanett Wheeler, *An Elliptic Collocation-Finite Element Method with Interior Penalties*, SIAM Journal on Numerical Analysis, 15 (1978), pp. 152–161.

[56] M. Windhoff, Opitz A., and Thielscher A., *Electric field calculations in brain stimulation based on finite elements: an optimized processing pipeline for the generation and usage of accurate individual head models.*, Hum Brain Mapp., 34 (2013), pp. 923–35.

[57] C. H. Wolters, L. Grasedyck, and W. Hackbusch, *Efficient computation of lead field bases and influence matrix for the FEM-based EEG and MEG inverse problem*, Inverse Problems, 20 (2004), pp. 1099–1116.

[58] C. H. Wolters, H. Köstler, C. Möller, J. Härdtlein, and A. Anwander, *Numerical approaches for dipole modeling in finite element method based source analysis.*, International Congress Series, 1300 (June 2007), pp. 189–192. ISBN-13:978-0-444-52885-8, http://dx.doi.org/10.1016/j.ics.2007.02.014.

[59] C. H. Wolters, H. Köstler, C. Möller, J. Härdtlein, L. Grasedyck, and W. Hackbusch, *Numerical mathematics of the subtraction method for the modeling of a current dipole in EEG source reconstruction using finite element head models*, SIAM Journal on Scientific Computing, 30 (2007), pp. 24–45.

[60] Y. Yan, P. L. Nunez, and R. T. Hart, *Finite-element model of the human head: scalp potentials due to dipole sources*, Medical and Biological Engineering and Computing, 29 (1991), pp. 475–481.